ELSEVIER

International Journal of Mass Spectrometry 189 (1999) 157–171

International Journal of Mass Spectrometry

On the formation of ionic species generated in UV-laser desorption ionization of a frozen aqueous $CeCl_3$ solution

Chau-Chung Han*, Ying-Lai W. Han, Yao-Chien Chen

Institute of Atomic and Molecular Sciences, Academia Sinica, P.O. Box 23-166 Taipei, Taiwan, People's Republic of China

Received 14 November 1998; accepted 23 April 1999

Abstract

The 266 nm laser desorption ionization of frozen $CeCl_3/D_2O$ solutions at power densities of about 3×10^8 W/cm^2 is studied. Characteristic ionic species desorbed include D_2O^+, $D_3O^+ \cdot (D_2O)_{0-5}$, Ce^+, CeO^+, and $CeO^+(D_2O)_n$. Large quantities of D_2O vapor are released for an extended period of time. The velocity distributions of these species are analyzed to provide insight into their formation mechanisms. The hydrated metal ion in the frozen bulk sample absorbs the excitation photon and initiates an explosive desorption that ejects, among other species, a CeO^+ ion that then becomes a nucleation core onto which water molecules are sequentially attached. Energy relaxation into the ice matrix induced water evaporation/sublimation that lasted for 300 μs after the 10 ns laser pulse. The experimental data strongly suggest that $CeO^+(D_2O)_n$ are formed through a condensation mechanism instead of arising from dissociation of directly desorbed higher hydrates. The energy-sink role of the ice matrix and its low critical temperature in vacuum resulted in the release over a prolonged period of a very slowly drifting atmosphere of D_2O vapor that acts to retard the explosively ejected CeO^+ core ions through D_2O pickup/condensation and unreactive inelastic collisions. (Int J Mass Spectrom 189 (1999) 157–171) © 1999 Elsevier Science B.V.

Keywords: Hydrated ions formed in laser desorption ionization; Laser desorption ionization from a frozen aqueous sample; Condensation in a laser ablated plume

1. Introduction

In addition to those naturally existing transition metal and rare-earth complexes, new compounds are being synthesized in the laboratory for purposes such as the development of new reagents and catalysts, modification, and production of materials with desired new or special properties, etc. Transition metal complexes had in the past played a long-reaching role in establishing our knowledge of chemical bonding. Many of these metal complexes are ionic and become conducting electrolytes when dissolved. Many of them contain metal atoms either in ill-defined or in very high oxidation states. In the case of rare-earth complexes, our knowledge is far less complete than that of *d*-orbital transition metal complexes. Mainstream studies of (ionic) transition metal complexes have been limited to the condensed phase, and because of their lack of vapor pressure and/or thermal stability they have received little gas-phase study. Generation of gas-phase transition metal complex ions was demonstrated in the 1980s with the advent of particle impact-induced [1–3] and laser desorption

* Corresponding author. E-mail: cchan@po.iams.sinica.edu.tw

PII S1387-3806(99)00071-8

ionization techniques [4], but very limited progress has been made in gas-phase studies over the past decade. Electrospray ionization has recently opened a promising route to gas phase study [5–16].

Laser desorption ionization (LDI) and its close relative, matrix-assisted laser desorption (ionization) [MALD(I)], have now become one of several popular and routinely applied analytical techniques for the vaporization (and ionization) of thermally unstable or nonvolatile compounds. Water is the most versatile, friendly, and powerful solvent in common use and it is closely tied to living organisms. A number of research teams have demonstrated the desorption of materials from frozen aqueous samples. Rabalais [17] and his co-workers used energetic (0.5–3 keV) particle beams to induce secondary ion emission from water–ice surfaces and observed protonated water clusters composed of more than 50 molecules. Michl and his co-workers used similar techniques on matrix isolated organic as well as other condensed low-temperature samples [18,19].

Nelson and Williams demonstrated the ablation of high molecular weight DNA molecules from frozen aqueous solutions by laser ablation with 581 nm photons [20,21]. They etched the copper substrate to induce rust formation and the rust very likely acted as the chromophore that absorbed the 581 nm photons they used in their laser ablation experiments. Although their ensuing progress seemed not to have been very smooth (likely due to difficulties in controlling the property of the copper rust layer that might have been the key to the success of their experiments) Williams firmly advocates the continued exploration of laser ablation from frozen aqueous DNA solutions [21].

Belov et al. used a pulsed CO_2 laser for ablation from frozen solutions of organic molecules and postionized the organic vapor with a second tunable laser via a resonance-enhanced multiphoton ionization (REMPI) process [22]. Very recently, Hillenkamp et al. finally made exciting and significant progress in IR-LDI from water–ice that contained dispersed protein samples with 2.94 μm radiation [23]. Zare and his research team developed a method for desorbing samples injected into a mass spectrometer through a continuous liquid feed interface that may evolve into a highly sensitive detection system for some form of chromatographic separation techniques or capillary electrophoresis devices [24]. Although the absorption cross section of water at 1.9 μm is only 5% that of the commonly used UV matrix material nicotinic acid, Zare et al. have successfully demonstrated the detection of molecular ions of bovine insulin.

The potential of laser mass spectrometry with a frozen water matrix for environmental and bio-organic applications has been nicely demonstrated recently by the joint efforts of a Russian and British research group [25–27]. They used a pulsed 10.6 μm CO_2 laser as the ablation light source, and they reported that the rotational and translational temperatures of the desorbed phenol molecules initially embedded in an ice matrix were approximately 140–150 K, because of the cooling effect of the ejected water plume.

The combination of the solubility of ionic metal complexes in water with laser vaporization techniques has inspired our curiosity and interest in developing a LDI tool for gas-phase studies of ionic transition metal complexes. We choose $CeCl_3$ in this study for two reasons. First, it has several absorption bands in the UV region covering 200–275 nm that will eventually allow us to study wavelength effects with laboratory UV laser systems, and the strong water O–H stretching vibrational mode in the mid-IR can also be excited with a difference frequency crystal (to induce vaporization effects) and compared to results obtained with UV excitations. However, in this article we will only present results obtained with 266 nm excitation and results obtained with other wavelength photons will be reported in the near future when our laser system is expanded to cover the desired wavelength regions.

Second, each Ce^{III} atom in the bulk sample nominally carries seven ligated lattice water molecules that will likely bring about interesting charge redistribution phenomenon or redox reactions in an environment with reduced solvation. However, the exact solvated structure of the photoactive chromophore can be a lot more complicated than the chemical formula suggests, as is reflected by the existence of many

different crystallographic structures of highly coordinated Ce^{III} complexes. Typical aquo lanthanide ions M^{3+} are hydrolyzed in water, but this hydrolysis channel accounts for only about 1% in the case of Ce^{3+} and the main equilibrium has been reported to be [28]

$$3\ Ce^{3+} + 5\ H_2O \rightleftarrows [Ce_3(OH)_5]^{4+} + 5\ H^+$$

Lanthanides have a very high affinity for oxygen ligands and this is apparently the driving force for the exclusive formation of the CeO^+ core ion observed in our experiment.

2. Experimental

A commercially available $CeCl_3 \cdot 7H_2O$ sample (99%) is used without further purification. Fifteen μl aliquots of a 0.01 M solution, either in H_2O or D_2O, are applied to a 5-mm-diameter recess on the tip of a homemade low-temperature sample probe under a dry nitrogen atmosphere. The sample is then frozen by forcing a 4 ~ 5 l/min stream of liquid-nitrogen-cooled N_2 gas through the heat exchanging chamber at the low-temperature sample probe tip, however, the exact temperature of the sample is not measured. The ice layer thus formed has an average thickness of approximately 0.8 mm. Compared with LDI experiments using dried room-temperature samples, LDI from frozen aqueous solutions of a number of ionic metal complexes we have so far tested consistently resulted in more stable signals, and the frozen samples were more durable with respect to radiation damage.

LDI experiments are performed with the same home-built reflectron time-of-flight mass spectrometer reported previously in similar experiments [29]; a schematic presentation of the ion source configuration can be found therein. The desorption laser beam irradiates the sample surface at normal incidence. In electron impact ionization (EI) detection of a neutral D_2O vapor, a sheet of ionizing electrons emitted from a homemade electron gun containing the desorption laser axis intercepts the desorbed plume at the ion extraction volume. An optimized signal is obtained when the electron energy is set at about 300 eV. Directly desorbed ionic species drifting into the sampling zone or ions generated by EI of neutral precursors in the ion sampling volume of the mass spectrometer are analyzed at various delay times with respect to the desorption laser pulse by applying two synchronously pulsed high voltages to the Wiley–McLaren-type ion extraction electrodes flanking the ion sampling volume. These extraction electric fields accelerate the ionic species perpendicular to their desorption axis and into the time-of-flight mass spectrometer for mass analysis.

The 266 nm photon pulses are generated from a Lumonics HY750 Nd:YAG laser with a flat-topped intensity profile and a full width at half maximum (FWHM) pulse duration of approximately 8 ns. The laser beam is steered into the laser desorption ionization source region with a series of right-angle UV-quartz prisms and finally focused with a translatable 25 cm focal-length lens. The focal spot size is adjusted by varying the distance from the focusing lens to the sample surface. The optimum optical conditions are chosen by maximizing the hydrated ion signals. Qualitatively reproducible shot-to-shot ion signals are obtained when a laser beam energy of 2.5 ± 0.1 mJ/pulse, measured with a Scientech P25 pyroelectric power meter, is focused to about 1.1×10^{-3} cm^2 on the sample surface, corresponding to an average power density of $(2.8 \pm 0.1) \times 10^8$ W/cm^2. The laser is fired at a fixed repetition rate of 4 Hz and under this experimental condition there were no observable pressure jumps upon irradiation.

The photon intensity used in this current study is roughly one to two orders of magnitude above the desorption ionization threshold. In contrast to our previous report performed with a 10-fold lower laser intensity where sample preconditioning with up to 10 laser shots was necessary to start generating gas-phase ions [29a], ion signals are observed upon the first laser shot with the present power density level on a newly irradiated sample spot. Even so, we preconditioned each newly prepared frozen sample by irradiating it with some 10^3 laser shots across the sample surface before data acquisition started. Preconditioned samples yielded more stable signals in the early part of the experiment; this may have to do with the generation

of defects or color centers that assist and stabilize later photon absorption. We also observed that although the ion signals for Ce^+ and CeO^+ from a given sample spot maintain a reasonably constant level for >3000 laser shots, the hydrates display very similar decay with radiation dosage (vide infra, for example, see Fig. 6). After some 10^3 laser shots have been fired at a fixed sample spot, a shallow crater can usually be observed by the naked eye.

It has been experienced by all LDI and MALD(I) practitioners that ion signal intensities vary from shot to shot and from spot to spot across the sample surface. This has usually been ascribed to sample inhomogeneity and/or laser power fluctuation. Sample inhomogeneity is evidenced by the widespread variation in Na^+ and K^+ signals, which are usually among the most intense peaks in LDI mass spectra, with sampled spot and with radiation dosage. In order to average out possible inhomogeneity the sample is constantly rotated so that consecutive laser shots sampled different surface sites, unless otherwise stated, and we take 10 mass spectra at each delay time from 10 different sample spots before moving on to the next preprogrammed delay. In each run of an experiment, 5 delay-time-scan cycles are performed to step through the time window (1–50 μs) over which ion signals are detected and 50 mass spectra (10 from each of the 5 scans) so obtained at a common delay time were extracted and averaged to form the basis from which one set of temporal profile for all ionic species of interest is reconstructed. To assure self consistency of the experiment, 5 to 8 runs, each consisting of 5 repetitive delay-time scans, were obtained with one sample, and these 5 to 8 temporal profiles were compared against one another. They were then used to produce averaged temporal profiles and standard deviations for that particular sample. Experiments were repeated with 5 different samples prepared under similar conditions, and these 5 sets of temporal results are used to generate the final temporal profile of each ionic species and for estimating the overall experimental accuracy.

LDI with 355 nm and 532 nm photons has also been tried. Highly unstable signals and overall irreproducible velocity profiles are obtained at the former UV wavelength, although at the visible wavelength only sporadic ionic signals can be detected, even at significantly higher photon intensities. These trials reflect the positive correlation of sample absorption cross sections on the effectiveness of the LDI process. Only results obtained with 266 nm photons will be presented in this article.

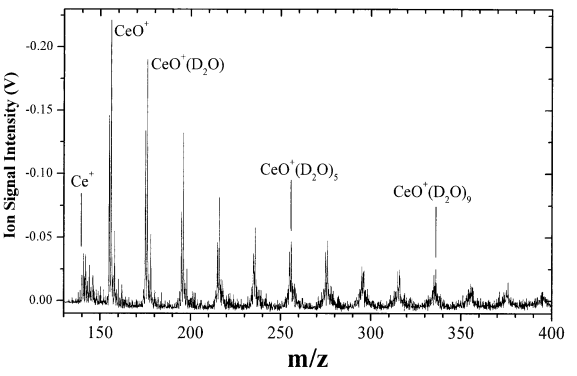

Fig. 1. Typical time-of-flight mass spectrum obtained by 266 nm laser desorption ionization from a 0.01 M frozen aqueous solution of $CeCl_3$ at a photon density of about 2.7×10^8 W/cm^2.

3. Results and discussion

Fig. 1 shows a typical mass spectrum obtained from a frozen sample of 0.01 M $CeCl_3$ dissolved in D_2O. This spectrum contains Ce^+ (*m/z* 140/142), CeO^+ (*m/z* 156/158), and $CeO(D_2O)_n^+$ (*m/z* 156/158 + 20 × *n*) with $n = 1 \sim 11$. Except for the occasional weak Ce^{2+} signals, no other multiply charged ions can be unequivocally identified in the mass spectra. The generation of dominantly singly charged transition metal complex cations by various particle impact and photon-induced desorption techniques has been noted in most previous related reports. The lanthanide elements are known to have a very high affinity for oxygen ligands, and this property alone can account for the dominant formation of $Ce^{III}O^+$ instead of the $Ce^{III}Cl_2^+$ core ion, as well as the tendency to form hydrated cluster ions. Mass peaks at $m/z = 155 + 20 \times n$ are due to unidentified species. Not shown in Fig. 1 is the lower mass region that contains the following identifiable species: Na^+, K^+,

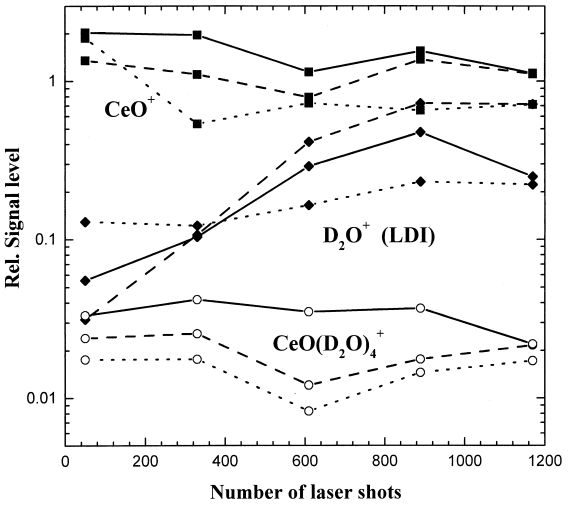

Fig. 2. Variation of LDI signal intensities of CeO^+ (solid square), D_2O^+ (solid diamond), $CeO^+(D_2O)_4$ (open circle) as a function of radiation dosage taken from three different constantly rotating frozen samples. Each ionic species is measured at a specific delay time after the laser pulse that corresponds to its maximum signal intensity and is the average of ten consecutive laser shots. The styles of the connecting lines represent the three independently prepared samples.

H_2O^+, D_2O^+, and $D_3O^+ \cdot (D_2O)_{0-5}$. The $CeO^+(D_2O)_n$ series of hydrated ions are unambiguously identified by mass increments of 18 versus 20 μ in the corresponding LDI mass spectra, obtained with samples dissolved in H_2O and D_2O, respectively. Although the commercial sample contains seven crystalline H_2O molecules for each Ce^{III} atom, only traces of H_2O are present in the gas-phase hydrates of CeO^+ when D_2O is used as the solvent. This is consistent with the 800-fold excess of D_2O over H_2O in the 0.01 M solution, and facile ligand exchange is suggested. It is worth mentioning that no sign could be identified for the existence of a "magic" hydration number in this and our previous article [29a]. This suggests that the stepwise hydration free energy change $\Delta G_{n-1,n}$ varies slowly and smoothly with n and there is not a clear-cut closing of a first hydration shell.

Fig. 2 shows the signal variation of three representative ionic species as a function of the number of laser shots fired for three independently prepared samples under constant rotation. The signal intensities represent the temporal signal maxima of each respective species. Results obtained for each of the three independently prepared samples are represented by different styles of the lines connecting the data points. For CeO^+ and $CeO^+(H_2O)_4$, the signal intensity variations are of a typical random fluctuation type. Interestingly, the laser desorbed D_2O^+ signal level showed a general increasing and final leveling-off trend with radiation dosage; no other ionic species showed a similar trend. The significance and cause of this special behavior in the D_2O^+ signal with the radiation dosage delivered to a sample awaits further investigation, but we currently suspect that it is somehow related to the extent of radiation damage in the sample that directly affects the efficacy of energy coupling from the radiation field to the ice lattice.

In addition to unavoidable pulse-to-pulse photon flux fluctuations, the variation in experimentally observed LDI signal intensities between different irradiated spots of the same sample and between different samples is most likely related to sample inhomogeneity arising from solvent–solute segregation during freezing of the aqueous solution. Instead of trying to characterize the frozen samples by a technique other than LDI-MS itself, we tried preparing the frozen sample by pneumatic spraying of the solution at a sample feeding rate of approximately 5 μL/min onto a precooled sample probe with the belief that this alternative sample preparation procedure would minimize the solvent–solute segregation problem during freezing. However, this latter method did not noticeably improve the signal stability and reproducibility when compared to the much more straightforward sample preparation procedure described in the experimental section. With either sample preparation method, we do not really have precise knowledge of, and control over, the actual local sample concentration, either because of the nature of freezing of a bulk solution under a dry nitrogen atmosphere in one case, or uncontrollable (and hard to calibrate) solvent evaporation during aerospray in the other case. What we can be sure of from the similar extent of signal stability observed with samples prepared by both methods is that the freezing rate of a 15 μl aliquot of sample solution is fast enough so that the salting-out effect does not significantly affect the results of our experiments.

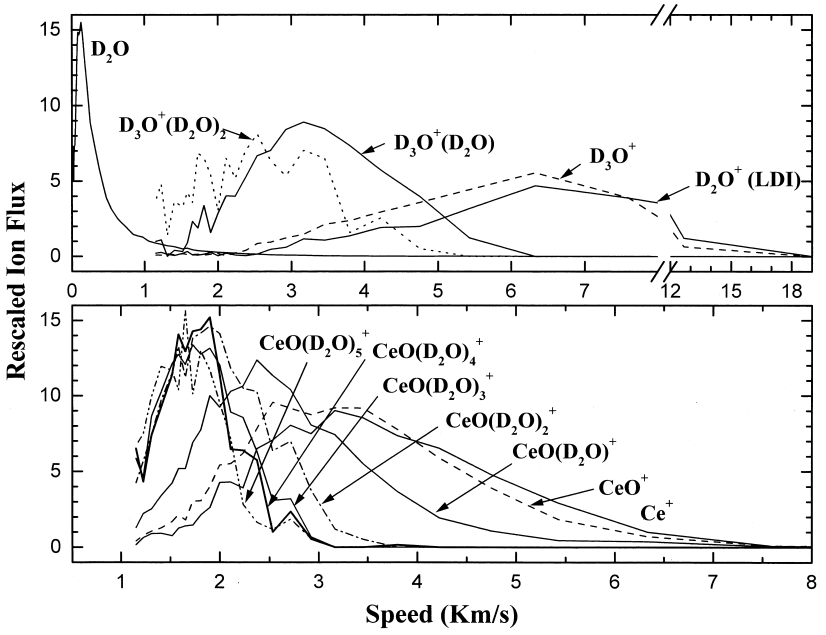

Fig. 3. Rescaled ion flux velocity distribution functions $f(v)$ vs. ion velocity v of some ionic species of interest. The amplitudes of the curves do not reflect the relative ion populations when different curves are compared due to data normalization before making further data treatments.

The experimentally measured ion signal intensities represent the populations of ions with different *m/z* values being sampled in the ion source region at each time delay after the firing of the laser. Thus, this observable is proportional to the ion densities inside the ion sampling volume at the moment of ion extraction. The data treatment algorithm used by Zare et al. [30] is applied to analyze our experimental temporal signal variation. Because different samples yielded sizable variations in absolute signal level, the experimentally observed ion density-related signal $g_{\text{den}}(t)$ from each independently prepared sample is first normalized to have a peak intensity level of 1 for each ionic species, and then converted into an ion flux-related velocity distribution function $f(v)$ using the following relationship:

$$t \cdot g_{\text{den}}(t) \propto f(l/t) = f(v) \propto v^3 \exp\left(-\frac{mv^2}{2kT}\right) \qquad (1)$$

where l is the free-drift distance from the sample to the ion sampling volume, which is 38 mm in the current experiment, and t is the delay time of ion extraction with respect to laser firing. The flux-related distribution functions $f(v)$ will later be used to calculate averaged ion kinetic energies. The 5 to 8 $f(v)$ curves of a given *m/z* ion obtained from a sample are then compared against each other for self consistency and averaged to give the representative $f(v)$ for that particular sample. Five sets of independent measurements obtained for five different samples are finally combined to give the net $f(v)$ and standard deviation. Fig. 3 shows the corresponding $f(v)$ versus v profiles for ionic species of interest. As a result of normalization of the raw velocity distribution profiles before data averaging, the amplitudes of the curves shown in Fig. 3 do not reflect the relative ion populations when different curves are compared. The right-most term in Eq. (1) is the Maxwell–Boltzmann velocity distribution function for flux-sensitive detectors. After converting the raw experimental quantity $g_{\text{den}}(t)$ into $f(v)$, the ion-flux data is fitted to the following modified Maxwell–Boltzmann velocity distribution function

$$f(v) = a_1 \cdot v^3 \cdot \exp\left[-a_2 \cdot (v - a_3)^2\right] \quad (2)$$

Here, a_i are the adjustable parameters in the fitting procedures, and a_3 is usually termed the stream-velocity (V_s), which describes the center-of-mass flow of the system, in analogy to that found in molecular jets generated from a nozzle, whereas a_2 is related to a phenomenological temperature T_s through

$$T_s = \frac{m}{2 \cdot k_B \cdot a_2} \quad (3)$$

where m is the mass of the ionic species being studied and k_B the Boltzmann constant. In laser desorption processes, the stream velocity term is ascribed to near-surface collisions [31]. Under our experimental conditions, the solute absorbs with a moderate cross section at the photon wavelength [29a], and large quantities of water vapor are generated through rapid energy redistribution so that a Knudsen layer [32] guarantees frequent near-surface collisions, therefore, a modified Maxwell–Boltzmann distribution function [i.e. $a_3 > 0$ in Eq. (2)] is anticipated to be more appropriate for describing our experimental $f(v)$'s. Indeed, data fitting incorporating a stream-velocity term consistently yielded significantly better fits to our data. Displayed in Fig. 4 are three representative fitted curves to experimental results; the vertical bars represent one standard deviation based on five sets of independent experiments, each using a newly prepared frozen sample. The numerical results extracted from the fitting procedures along with average and most probable kinetic energies are summarized in Table 1.

From the results presented in Fig. 3 and Table 1, it is quite apparent that Ce^+, CeO^+, D_2O^+, and D_3O^+ generated in direct laser desorption ionization behave distinctly different from the higher hydrated ions $CeO^+(D_2O)_{1-5}$ and $D_3O^+(D_2O)_{1-2}$. All of these desorbed ionic species have peak velocities well over 1 Km/s. Ionic velocities of this magnitude are unusual for typical MALD(I) experiments, yet quite common in laser ablated metallic plumes. On the other hand, desorbed neutral D_2O molecules, also detected with electron impact ionization as D_2O^+, are much slower (most probable velocity $V_{mp} \simeq 130$ m/s) than all the other species detected in this work, and this is the only species that could not achieve a satisfactory fit by the Maxwell–Boltzmann distribution functions. According to the best nonlinear least-squares fitting results summarized in Table 1, Ce^+ and CeO^+ share the same stream velocity of about 1.8 km/s, and the same nominal temperature of approximately 30 000 K. Although D_2O^+ generated by direct LDI also has this same phenomenological temperature, it is characterized by a notably faster nominal stream velocity (best-fitted value of 2.6 km/s) than the corresponding values for Ce^+ and CeO^+ ($\approx$1.8 Km/s). It is interesting to note that D_3O^+ also has the same best nonlinear least-squares fitted stream velocity as that of D_2O^+, nevertheless, D_3O^+ has a significantly lower phenomenological temperature of 22 000 K versus that of

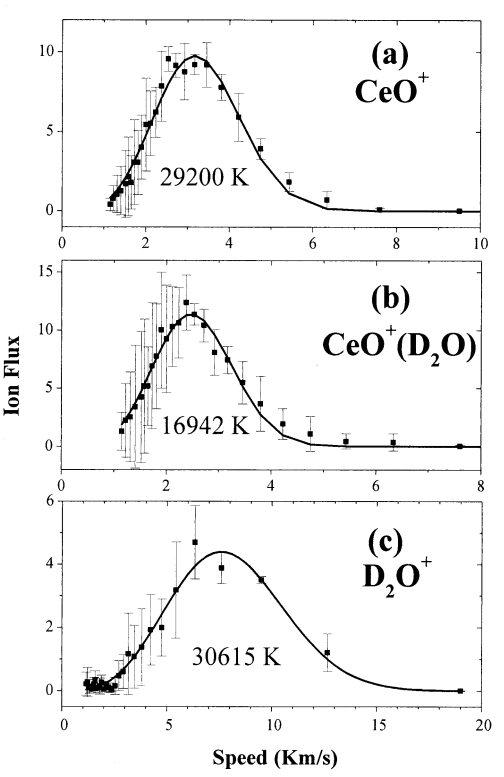

Fig. 4. Best nonlinear least-squares fitting of experimental velocity distributions to modified Maxwell–Boltzmann functions. (a) CeO^+, (b) $CeO^+(D_2O)$, and (c) D_2O^+ generated by direct laser desorption ionization (i.e. without EI). The best fitting parameters are summarized in Table 1.

Table 1
Best parameters obtained from nonlinear least-squares fitting of experimental velocity distributions to (modified) Maxwell–Boltzmann distribution functions

m/z	Composition	V_s (Km/s)	Temp.	$\langle E_k \rangle$ (eV)[c]	$E_{k,mp}$ (eV)[d]
20(LDI)	D_2O^+	2.6 ± 0.7	30600	7.41	5.99
22	$(D_3O)^+$	2.6 ± 0.4	21800	5.76	4.52
140	Ce^+	1.8 ± 0.2	30400	9.96	8.67
156	CeO^+	1.7 ± 0.1	29200	9.55	8.12
20(LDI)	D_2O^+	1.8[a]	36000[a]	7.67[a]	5.99
22	$(D_3O)^+$	1.8[a]	27000[a]	6.03	4.97
20 (LDI)	D_2O^+	1.8[b]	30000[b]	6.54[b]	5.99
22	$(D_3O)^+$	1.8[b]	30000[b]	6.62	5.43
42	$(D_3O)^+(D_2O)$	2.2 ± 0.1	6600	2.75	2.33
176	$CeO(D_2O)^+$	1.51 ± 0.09	17000	6.41	5.86
196	$CeO(D_2O)_2^+$	1.23 ± 0.07	10100	4.16	3.14
216	$CeO(D_2O)_3^+$	1.29 ± 0.04	7400	3.85	3.46
236	$CeO(D_2O)_4^+$	1.43 ± 0.04	5100	3.97	3.65
256	$CeO(D_2O)_5^+$	1.25 ± 0.07	6400	3.85	3.62

[a] Stream velocity is set at 1.8 km/s in a separate fit. Refer to Fig. 5(a) and (c). The corresponding fitted best temperatures are noted on the respective figures.

[b] Both stream velocity and temperature are set at these specified values and the simulated velocity distribution curve still agrees with our data within experimental error. Refer to Fig. 5(b) and (d).

[c] $\langle E_k \rangle$ represents average ion kinetic energy.

[d] $E_{k,mp}$ represents the most probable ion kinetic energy that corresponds to the peak maximum of each respective $f(v)$ curve.

D_2O^+ (30 600 K). However, the relatively large uncertainties in the fitted stream velocities for both D_2O^+ and D_3O^+ reflect the intrinsically deteriorating velocity resolution toward higher velocity particles in our experimental scheme; the numerical results obtained for fast D_2O^+ and D_3O^+ have to be interpreted with more caution. Within our experimental uncertainty, the LDI generated D_2O^+ and D_3O^+ velocity distribution profiles can also be described by the same set of stream velocity and/or nominal temperature as those of Ce^+ and CeO^+, as shown in Fig. 5(b) and (d), respectively.

The similarity in hydrodynamic properties among LDI generated D_2O^+, D_3O^+, Ce^+, and CeO^+ strongly suggests their common origin in the LDI process. Had a photothermal desorption mechanism been operative, the phenomenological temperature of 30 000 K would seem unreasonably high because this temperature is far above the critical temperature of water in vacuum. Based on existing experimental evidence regarding LDI processes, one would expect that rapid water sublimation, melting, and subsequent evaporation should have clamped the temperature of the system at a much lower level [33,34]. Thus, an alternative mechanism must be sought in order to account for our observations. A possible simple mechanism is that the surface chromophoric ligated metal ion, $Ce^{III}(D_2O)_xCl_y^{(3-y)+}$, or $[Ce_3(OH)_5]^{4+}$ (vide supra) absorbs the desorption UV photon through an electronic excitation transition into a repulsive state followed by immediate repulsive expulsion into the gas phase. A photon intensity of 10^8–10^9 W/cm^2 is generally accepted as a ball park value for the plasma ignition threshold [35,36]. The fitted temperature of 30 000 K may very likely suggest the formation of a hot plasma arising from photon absorption by the opaque plume near the surface. The incipiently ejected parent hydrated ion, whatever its exact chemical composition and charge state, may then further fragment into D_2O^+, D_3O^+, Ce^+, and CeO^+; these small secondary fragment ions then all acquire the characteristic local temperature of the hot plasma as well as the ballistic stream velocity of the incipiently ejected parent ion. This hypothesis can account for the same hydrodynamic characteristics observed for these species. This ion formation

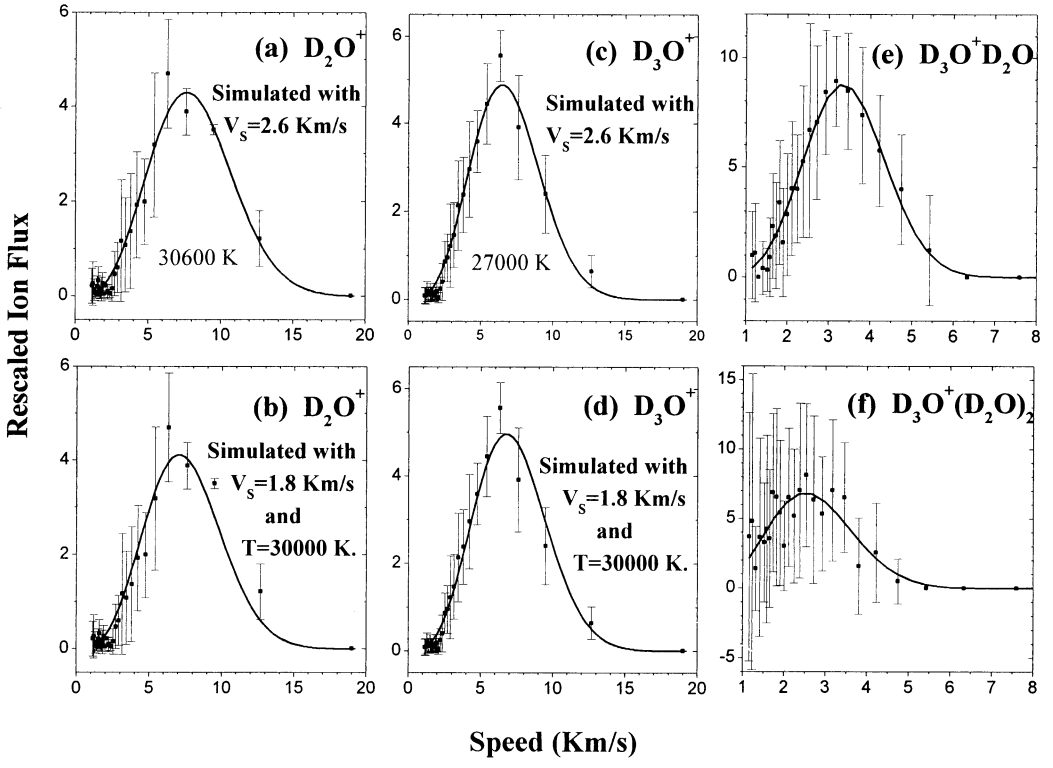

Fig. 5. D_2O^+ generated by LDI (i.e. without EI) with different fitting parameters: (a) best-fitted results with no constraints set forth on the parameters a_1, a_2, and a_3 in Eq. (2). The corresponding phenomenological temperature obtained from Eq. (3) is 30 600 K, (b) simulated velocity distribution curve with enforced stream velocity of 1.8 km/s and a temperature of 30 000 K. Corresponding best-fitted and similarly constrained fitting results for D_3O^+ are shown in (c) and (d), respectively. (e) and (f) are best-fitted results for $D_3O^+(D_2O)$ and $D_3O^+(D_2O)_2$, respectively.

mechanism is different from a gas-phase Coulomb explosion induced by the loss of solvation stabilization upon desolvation of a multiply charged core complex ion [such as $Ce(H_2O)_x^{3+}$, $CeCl(H_2O)_y^{2+}$ or even $[Ce_3(OH)_5]^{4+}$], because in this latter case all the fragments would display similar velocity distribution instead of similar hydrodynamic parameters (stream velocity and characteristic temperature).

As for the hydrated species $D_3O^+(D_2O)_{1–2}$ and $CeO^+(D_2O)_{1–5}$, they shift to increasingly reduced speeds with increasing mass (Fig. 3). This behavior apparently disagrees with a picture in which they had all originated from the fragmentation of a larger internally excited metastable cluster ion on its flight from the sample surface to the ion-sampling zone. In other words, our experimental results strongly suggest an alternative to the picture in which LDI incipiently generated large and internally excited $D_3O^+(D_2O)_x$, $CeO^+(D_2O)_x$, or even $[Ce_3(OD)_5(D_2O)_x]^{4+}$ hydrates that relax by evaporative cooling. Rather, two alternative models can qualitatively interpret our data. First, the large hydrated clusters are directly ejected with high speeds in the LDI process and the higher clusters are simply slowed down more by the slowly expanding water atmosphere as a result of their larger collisional cross sections. Although this model can correctly account for the observed reduction in stream velocity with the size of the hydrate, a concomitant broadening of velocity distribution, i.e. an increase in the characteristic temperature with hydrate size should occur, which is contrary to our experimental observation. Alternatively, our observations also fit a

picture where the D_2O^+, D_3O^+, and CeO^+ ion cores generated in an explosive photochemical process as outlined in the previous paragraph, pick up water molecules from the slowly expanding (vide infra) dense layer of water cloud formed by the same desorption laser pulse. In a first approximation, each of the successive nucleation steps will reduce the velocity of the growing cluster ion by a predictable amount, determined by the law of conservation of momentum that we will shortly show to predict a concomitant reduction in temperature with the extent of hydration. Based on this speculative mechanism, each subsequent nucleation is expected to retard the cluster system to a lesser extent as the hydrate grows in size, qualitatively reflecting what is observed in Fig. 3.

A qualitative insight into how the particle speeds vary with stepwise hydration can be achieved from a crude conservation of linear momentum calculation based on the aforementioned simple solvent pick-up model. Assuming that neutral D_2O molecules leave the surface with a mean stream velocity of 225 m/s (vide infra) and that D_2O^+, D_3O^+, and CeO^+ ion cores possess a most-probable ballistic speed (V_{mp}) of 7500, 6600, and 3167 m/s, respectively, as obtained from the best least-squares fitting of the experimental data shown in Figs. 4 and 5. A deuterium atom transfer resulting from D_2O^+ colliding with a spectator D_2O molecule is expected to acquire a reduced D_3O^+ velocity of 6839 m/s, in satisfactory consistency with the observed peak speed of 6600 m/s for D_3O^+. Similarly, this model predicts $V_{mp}(CeO^+) = 3123$ m/s, had CeO^+ been produced from the reaction of Ce^+ ($V_{mp} = 3455$ m/s, spectator) with D_2O ($V_s = 225$ m/s, spectator), again in close agreement with the experimentally determined value of 3167 m/s. Then, sequential attachment of 1 and 2 D_2O molecules to D_3O^+ will further reduce V_{mp} of the growing hydrated ions to 3564 m/s and 2487 m/s for $D_3O^+(D_2O)$ and $D_3O^+(D_2O)_2$, respectively. These values again agree surprisingly well with the experimentally observed peak values of 3300 and 2600 m/s for these first two hydrated hydronium ions shown in Fig. 5(e) and (f), respectively. From these results we can conclude that the simple model of stepwise hydration and conservation of linear momentum consideration can semiquantitatively account for our limited experimental results on $D_3O^+(D_2O)_x$. Based on this simple nucleation model, sequential nucleation of 1–5 D_2O molecules onto the CeO^+ ion core will result in the following peak velocities for $CeO^+(D_2O)_{1–5}$ ions: 2834, 2567, 2351, 2170, and 2018 m/s, respectively. We will denote the simple nucleation model described in this paragraph "model 1," in order to distinguish it from the slightly modified version to be discussed in the next paragraph.

Although the simple solvent pick-up model 1 presented in the previous paragraph already enjoyed semiquantitative success, it is not without flaw. There, energy relaxation after each nucleation step has not been explicitly considered. Here we make a slight modification to model 1 by assuming that the growth of hydrated ions involves a three-body process where an extra water molecule is responsible for carrying off the ion–water interaction energy, and this modified version will be dubbed "model 2." Because this model now involves momentum exchange with two slowly moving water molecules, the predicted most-probable energy will be lower than that predicted by model 1. The experimentally determined and theoretically predicted V_{mp} obtained with both nucleation models are summarized in Table 2.

From the results listed in Table 2, it appears that although model 1 underestimates the rate of decrease in V_{mp} with hydration size, model 2 overcorrected the trend. A long-lived three-body ion–$(water)_2$ complex implicit in model 2 is the cause for the excessive momentum removal by the departing water molecule. Therefore, a situation based on model 1 with allowance for partially inelastic collisions between the incipiently formed ion–water binary adduct with the dense water cloud to stabilize the adduct can conceptually depict the formation of the hydrated species.

The origins of D_3O^+ and CeO^+ cannot be unequivocally identified in our present experiment, as reflected from the numerical values shown in Table 2. Although we have chosen to treat them as if they were independently and directly formed in the LDI process, which receives support from the data presented in Fig. 6 (vide infra), we have no sound evidence to exclude

Table 2
Comparison of the most probable desorbed ion velocities (V_{mp}) obtained from experiments, and the two simple solvent pick-up models described in the text

Ion	V_{mp} (m/s, expt.)	V_{mp} (m/s, model 1)	V_{mp} (m/s, model 2)
D_2O^+	7500		
D_3O^+	6600	6839[a]	2487
$D_3O^+(D_2O)$	3300	3564	1384
$D_3O^+(D_2O)_2$	2600	2487	929
Ce^+	3455		
CeO^+	3167	3123[b]	
$CeO^+(D_2O)$	2533	2834	2567
$CeO^+(D_2O)_2$	1900	2567	2134
$CeO^+(D_2O)_3$	1757	2351	1810
$CeO^+(D_2O)_4$	1727	2170	1562
$CeO^+(D_2O)_5$	1652	2018	1369

[a] Value obtained by assuming D_2O^+ (V_{mp} = 7500 m/s) + D_2O (V_s = 225 m/s, spectator) → D_3O^+ + OD, under conditions of conservation of linear momentum.

[b] Value obtained by assuming Ce^+ (V_{mp} = 3455 m/s) + D_2O (V_s = 225 m/s, spectator) → CeO^+ + $2D/D_2$, under conditions of conservation of linear momentum.

their formation through reactions of D_2O^+/Ce^+ with D_2O. The experimentally measured V_{mp} values for D_3O^+ and CeO^+ are nearly identical with those predicted by model 1 assuming their generation through reactions of D_2O^+/Ce^+ with D_2O.

If we go one step further in analyzing our data by starting with the experimental CeO^+ velocity profile $f(v)$ to derive the simulated velocity distributions of $CeO^+(D_2O)_n$ based on the aforementioned conservation of linear momentum principle (model 1), we predict temperatures of 25 550, 22 650, 20 300, 18 400, and 16 800 K, and stream velocities of 1.6 ± 0.1, 1.5 ± 0.1, 1.4 ± 0.1, 1.3 ± 0.1, and 1.2 ± 0.1 Km/s, respectively, for $n = 1 \sim 5$. The stream velocities obtained from this more cumbersome simulation of the evolving velocity profiles after each attachment of D_2O parallel the experimentally derived trend summarized in Table 1. Although the trend of decreasing characteristic temperature parallels our

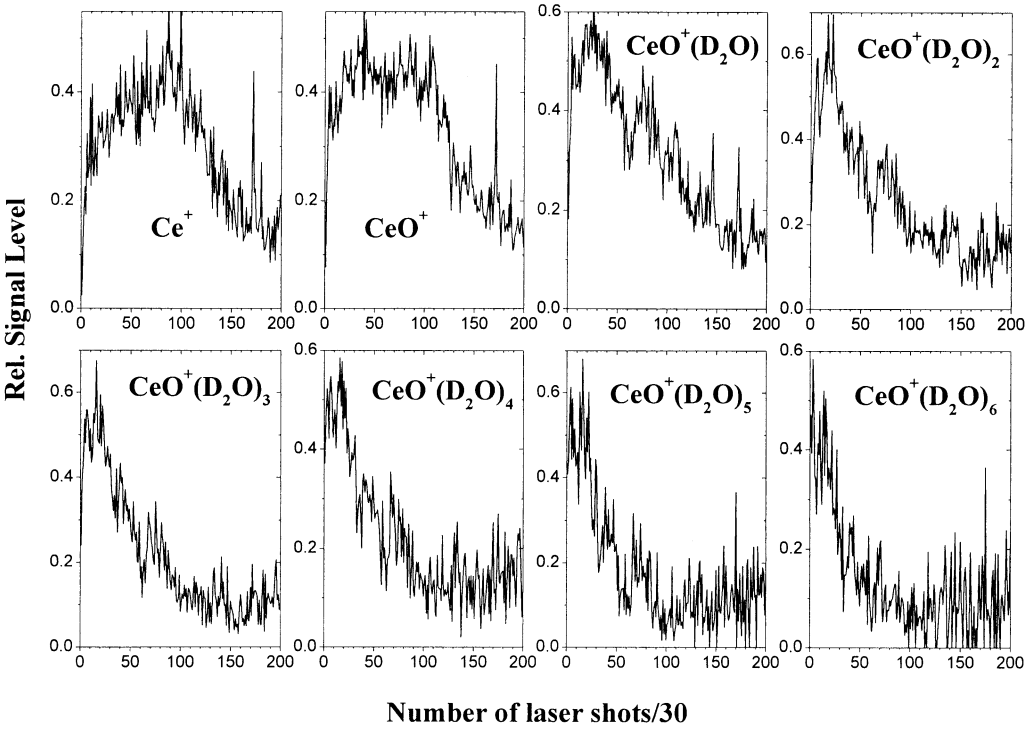

Fig. 6. Signal variation of a variety of ionic species as a function of radiation dosage delivered to a fixed sample spot. Each data point is the average of 30 consecutive laser shots. Whereas all the hydrated CeO^+ ions appear to have very similar signal variation profiles, $CeO^+(D_2O)$ displays a slight but detectably slower decay rate with radiation dosage than the other higher hydrates.

experimental observations, the predicted rate of cooling with increasing hydrate size is much too slow. This may be attributed to the fact that in the real world the probability for clustering increases for the low temperature portions of the precursor population, either because of improved interaction time or for simple energetic reasons. Alternatively, partially inelastic collisions not included in our oversimplified model 1 may also account for this discrepancy. In our opinion, the qualitative or even semiquantitative agreement in these characteristic temperatures and V_{mp}'s obtained from this oversimplified model 1 with those listed in Tables 1 and 2 provide support for the nucleation mechanism for the formation of $CeO^+(D_2O)_n$. Consistent with this picture, when this experiment was carried out on a linear TOF (time-of-flight)-MS instrument with continuous ion draw out (i.e. a static acceleration electric field constantly acts on the frozen sample), only feeble signals corresponding to the first few $CeO(D_2O)_x^+$ ions were observed. The latter LDI experiment is carried out in the presence of a strong ion extraction field so that the incipiently formed ionic cores are immediately separated from the neutral water vapor cloud and the probability of water condensation onto the ionic core is greatly reduced. However, the possible counteracting effect of collision-induced dissociation of hydrated species in this latter experimental setup cannot be excluded.

Finally, we comment on the nature of desorbed neutral water molecules. The experimental velocity distribution of this species cannot be fit satisfactorily to any reasonable modification of the Maxwell–Boltzmann distribution function. This can be accounted for by the fact that this fitting procedure implicitly assumes that the duration of particle emission is short compared to either the time resolution (μs in our experiment) or the drift time from the sample surface to the spot of particle density determination. As the emission of neutral D_2O molecules continue for $\approx$3 ms after the desorption laser pulse, our failure to satisfactorily fit its velocity distribution to the Maxwell–Boltzmann function is not too surprising. The long D_2O thermal emission time arises from the combination of two major physical properties of the system under study. First, the finite absorption cross section of the frozen sample at 266 nm [29a] entails a penetration depth that is considerably larger than encountered in typical resonance laser excitation desorption experiments from thick sample layers. Second, the small thermal conductivity of water, which is roughly three orders of magnitude smaller than typical metals, entails a long thermal relaxation time for photoexcited sample volumes at a distance from the solid–vacuum interface. Because of the lack of quantitative knowledge on the optical and thermal properties of our sample, a detailed numerical modeling of the thermal relaxation process applying the heat-conduction equation was not attempted. We simply point out that other examples can be found where desorption signal extends into the ms range [37].

Applying the algorithm developed in our previous work, we derived a relaxation time constant of 350 μs and an average speed of 225 m/s for the emission of neutral D_2O [29a]. To a first approximation, this 0.35 ms relaxation time can be viewed as the amount of time the irradiated spot needs to dissipate the local heat produced by the laser pulse. The slow stream velocity of the desorbed neutral D_2O vapor can be ascribed to a photothermal desorption process occurring at a relatively low effective surface temperature demanded by the low critical temperature of ice in vacuum and this clearly implies the benefit of using water ice as matrix material. Both water evaporation or sublimation and heat conduction will eventually bring the surface temperature at the irradiated spot back to a nonvaporizing level, and this cooling down takes about 350 μs in our case. The average velocity of neutral D_2O is much slower than the nominal stream velocity of the ionic species detected in this study and this appeared to be the opposite situation observed in typical MALD(I) processes, where the ejecting matrix molecules imparts kinetic energy to the embedded analyte molecule [38]. In our present case, the water matrix is not playing the role of a photon-absorbing chromophore at 266 nm; instead, it acts as a passive energy sink [39]. Its peculiarly slow gas-phase drifting behavior can be rationalized by considering that the D_2O atmosphere acts to buffer the

explosive ejection of the incipiently formed ionic species instead of acting in the conventional sense of being a carrier gas that imparts a stream velocity to the entrained particles.

Whereas all the experiments discussed above were carried out with the sample under constant rotation to expose new sample spots to consecutive laser shots, Fig. 6 displays the signal variation of a variety of ionic species emitted from a fixed sample spot as a function of radiation dosage. Here, each data point is the average of 30 consecutive laser shots, and therefore, these spectra are a record of signal variation over a total of 6000 laser shots being fired at a fixed sample spot. It is interesting to note that Ce^+ and CeO^+ display qualitatively identical dependence on radiation dosage imparted at a given sample spot. $CeO^+(D_2O)$ displays a notably slower decay rate with radiation dosage than the other higher hydrates where qualitatively identical rapid decays in their signal intensities are observed. Based on the cluster growth mechanism we proposed for the observed hydrates and the observed faster decay rates for the higher hydrates, the results shown in Fig. 6 as a whole can be interpreted as reflecting the decreasing $D_2O_{(g)}$ yield with radiation dosage delivered to a fixed sample spot. On the other hand, the very similar behavior of Ce^+ and CeO^+ seems to suggest their parallel and independent formation in the LDI process, because CeO^+ would otherwise be expected to display similar decay properties because the hydrates had their origin come from the bimolecular reaction between Ce^+ and D_2O.

The initial rapid increase in ion signal observed in Fig. 6 reflects the pertinence of the sample preconditioning procedure we took (see Sec. 2) before collecting velocity distribution data. Typical covalently bonded cluster systems generated by laser ablation processes, such as carbon, semiconductor, and metallic clusters, display an increased extent of clustering with the formation of a crater in the bulk solid target as a result of the accumulated laser drilling effect. This phenomenon has been ascribed to the confined ejection angle set by the crater that increased three-body collision probability and thus cluster formation. In our case, an opposite trend for the cluster population has been observed with the number of laser shots fired at a fixed spot. This can be the result of two physical processes. First, the low-melting temperature of the icy sample creates a shallow and widely open crater as opposed to the deep and narrow tunnel-like surface damage observed in high-melting samples; thus, the plume confinement effect is not as effective with radiation dosage as observed in the other high-melting materials. Second, even if there was plume confinement due to crater formation, it may not manifest itself for increased overlap of the 8 ns UV desorption laser beam with the desorbed plume that resulted in a heating effect.

4. Concluding remarks

We have provided experimental evidence that Ce^+, CeO^+, D_2O^+ and very likely D_3O^+ generated in 266 nm laser desorption ionization of frozen $CeCl_3$ solutions are directly formed under practically identical conditions initiated by electronic excitation of the hydrated metal complex ion chromophore in the bulk icy sample. The incipiently desorbed parent species, say, $Ce(D_2O)_x^{3+}$, $CeO(D_2O)_x^+$, or $[Ce_3(OH)_5(D_2O)_x]^{4+}$ undergo fragmentation within a possible plasma region to yield fragments sharing the same hydrodynamic characteristics. On the other hand, available evidence suggests that the hydrated species $D_3O^+(D_2O)_{1–3}$ and $CeO^+(D_2O)_{1–5}$ are formed through a nucleation route.

Water in the solid state is an ideal matrix material because its low critical temperature will act to clamp the highest system temperature achievable due to photothermal effects, and its effective gas phase cooling collisions with the entrained analyte molecules work to minimize further sample decomposition. In our present experiment, we have used our analyte sample (the metal salt) as the chromophore, a practice opposite to typical MALD(I) experiments. For this reason, we are setting up new experiments designed to excite the water O–H stretching vibration in the 3 μm region so as to utilize the majority of water molecules in the icy sample systems as a normal matrix. Ionization may be a problem in one-laser IR-LDI of neutral molecular samples but this may not

be a concern for ionic samples. In addition, photochemical reactions of the analyte molecules can be largely avoided by using IR radiation for desorption, thus eliminating complications arising from analyte absorption. These new experiments shall have the potential of resolving some of the shortcomings of the currently used UV-MALD(I) technique, and this direct excitation of the water mode in the ice matrix has potential applications in water quality monitoring and biomedical screening tests of body fluids and tissues.

The time-scanning nature of our current TOF-MS setup makes it very difficult to measure the photon fluence/intensity dependence of ion yields and velocity distributions. Experiments applying a quadrupole mass spectrometer that will allow us to register the complete velocity distribution profile and ion yield for each laser pulse for a selected ion are being planned, and more detailed studies promise better understanding of the dynamical details involved in the subject laser ablation process.

Acknowledgement

The funding for this work is provided by the National Science Council and the Chinese Petroleum Corporation of the Republic of China. Assistance in automation of experimental setup and data analysis from H.C. Lin is also gratefully acknowledged.

References

[1] J.M. Miller, K. Balasanmugam, Can. J. Chem. 67 (1989) 1496.
[2] J.L. Pierce, K.L. Busch, R.G. Cooks, R.A. Walton, Inorg. Chem. 22 (1983) 2492.
[3] J.L. Pierce, K.L. Busch, R.A. Walton, Organometallics 1 (1982) 1328.
[4] K. Balasanmugam, R.J. Day, D.M. Hercules, Inorg. Chem. 24 (1985) 4477.
[5] T.G. Spence, T.D. Burns, L.A. Posey, J. Phys. Chem. A 101 (1997) 139.
[6] T.D. Burns, T.G. Spence, M.A. Mooney, L.A. Posey, Chem. Phys. Lett. 258 (1996) 669.
[7] J.M. Curtis, P.J. Derrick, A. Schnell, E. Constantin, R.T. Gallagher, J.R. Chapman, Inorg. Chim. Acta 201 (1992) 197.
[8] J.M. Curtis, P.J. Derrick, A. Schnell, E. Constantin, R.T. Gallagher, J.R. Chapman, Org. Mass Spectrom. 27 (1992) 1176.
[9] R. Colton, J.C. Traeger, Inorg. Chim. Acta 201 (1992) 153.
[10] V. Katta, S.K. Chowdhury, B.T. Chait, J. Am. Chem. Soc. 112 (1990) 5348.
[11] A.T. Blades, P. Jayaweera, M.G. Ikonomou, P. Kebarle, Int. J. Mass Spectrom. Ion Processes 102 (1990) 251.
[12] A.T. Blades, P. Jayaweera, M.G. Ikonomou, P. Kebarle, Int. J. Mass Spectrom. Ion Processes 101 (1990) 325.
[13] P. Jayaweera, A.T. Blades, M.G. Ikonomou, P. Kebarle, J. Am. Chem. Soc. 112 (1990) 2452.
[14] A.T. Blades, P. Jayaweera, M.G. Ikonomou, P. Kebarle, J. Chem. Phys. 92 (1990) 5900.
[15] C.L. Gatlin, Tureček, in Electrospray Ionization Mass Spectrometry, Fundamentals, Instrumentation, and Applications, R. B. Cole (Ed.), Wiley, New York, 1997.
[16] R. Colton, A. D'Agostino, J.C. Traeger, Mass Spectrom. Rev. 14 (1995) 79.
[17] G.M. Lancaster, F. Honda, Y. Fukuda, J.W. Rabalais, J. Am. Chem. Soc. 101 (1979) 1951.
[18] H.T. Jonkman, J. Michl, R.N. King, J.D. Andrade, Anal. Chem. 50 (1978) 2078.
[19] T.F. Magnera, D.E. David, D. Stulik, R.G. Orth, H.T. Jonkman, J. Michl, J. Am. Chem. Soc. 111 (1989) 5036.
[20] R.W. Nelson, M.J. Rainbow, D.E. Lohr, P. Williams, Science 246 (1989) 1585.
[21] P. Williams, Int. J. Mass Spectrom. Ion Processes 131 (1994) 335.
[22] M.E. Belov, S.S. Alimpiev, V.V. Mlynsky, S.M. Nikoforov, P.J. Derrick, Rapid Commun. Mass Spectrom. 9 (1995) 1431.
[23] S. Berkenkamp, M. Karas, F. Hillenkamp, Proc. Natl. Acad. Sci. USA 93 (1996) 7003.
[24] E.R. Williams, G. C. Jones Jr., L.L. Fang, T. Nagata, R.N. Zare, SPIE Appl. Spectrosc. Mater. Sci. II 1636 (1992) 172.
[25] P. Kraft, S. Alimpiev, E. Dratz, J. Sunner, J. Am. Soc. Mass Spectrom. 9 (1998) 912.
[26] S.S. Alimpiev, M.E. Belov, V.V. Mlinsky, S.M. Nikiforov, Analyst 119 (1994) 579.
[27] S.S. Alimpiev, V.V. Mlinsky, M.E. Belov, S.M. Nikiforov, Anal. Chem. 67 (1995) 181.
[28] F.A. Cotton, G. Wilkinson, Advanced Inorganic Chemistry: A Comprehensive Text, Wiley, New York, 1972, 3rd ed., p. 1067.
[29] (a) H.M. Hung, C.C. Han, S.H. Lin, J. Cluster Sci. 6 (1995) 533; (b) S.-S. Ju, C.-C. Han, C-J. Wu, A.M. Mebel, Y.-T. Chen, J. Phys. Chem. B 103 (1999) 582.
[30] R. Zenobi, R.N. Zare, in Advances in Multi-Photon Processes and Spectroscopy, S.H. Lin (Ed.), World Scientific, Singapore, 1991, pp. 3–167.
[31] R. Kelly, R.W. Dreyfus, Surf. Sci. 198 (1988) 263.
[32] R. Kelly, Phys. Rev. A 4 (1992) 860.
[33] R.C. Beavis, J. Lindner, J. Grotemeyer, E.W. Schlag, Chem. Phys. Lett. 146 (1988) 310.
[34] R.C. Beavis, J. Lindner, J. Grotemeyer, E.W. Schlag, Z. Naturforsch A 43 (1988) 1083.
[35] A. Vertes, G. Irinyi, R. Gijbels, Anal. Chem. 65 (1993) 2389.

[36] A. Vertes, M.D. Wolf, P. Juhasz, R. Gijbels, Anal. Chem. 61 (1989) 1029.
[37] R. Braun, P. Hess, J. Chem. Phys. 99 (1993) 8330.
[38] R.C. Beavis, B.T. Chait, Chem. Phys. Lett. 181 (1991) 479.
[39] A similar experimental scenario has been reported for liquid solutions under atmospheric pressure: Y. Tsuboi, K. Hatanaka, H. Fukumura, H. Masuhara, J. Phys. Chem. 98 (1994) 11 237.